Journal of Computational Physics **180,** 229–255 (2002)
doi:10.1006/jcph.2002.7089

Discrete Singular Convolution–Finite Subdomain Method for the Solution of Incompressible Viscous Flows

D. C. Wan,* B. S. V. Patnaik,* and G. W. Wei*,†

**Department of Computational Science, National University of Singapore, Singapore 117543; and*
†Department of Mathematics, Michigan State University, East Lansing, Michigan 48824
E-mail: cscweigw@nus.edu.sg

Received November 13, 2000; revised December 7, 2001

This paper proposes a discrete singular convolution-finite subdomain method (DSC–FSM) for the analysis of incompressible viscous flows in multiply connected complex geometries. The DSC algorithm has its foundation in the theory of distributions. A block-structured grid of fictitious overlapping interfaces is designed to decompose a complex computational geometry into a finite number of subdomains. In each subdomain, the governing Navier–Stokes equations are discretized by using the DSC algorithm in space and a third-order Runge–Kutta scheme in time. Information exchange between fictitious overlapping zones is realized by using the DSC interpolating algorithm. The Taylor problem, with decaying vortices, could be solved to machine precision, with an excellent comparison against the exact solution. The reliability of the proposed method is tested by simulating the flow in a lid-driven cavity. The utility of the DSC–FSM approach is further illustrated by two other benchmark problems, viz., the flow over a backward-facing step and the laminar flow past a square prism. The present results compare well with the numerical and experimental data available in the literature.

I. INTRODUCTION

Over the past few decades, both the computational and experimental approaches to the numerical simulation of incompressible viscous flows have attracted great attention. This is primarily due to the wide industrial and engineering applications, and their relevance to complex flow phenomena, such as multiphase flows, and fundamental issues, such as turbulence. The governing Navier–Stokes equations are nonlinear and, in general, do not admit an analytical solution. For asymptotic parameter regions, analytical approaches and approximations are developed to improve the understanding of the nonlinear governing equations. For intermediate parameter regions, numerical computations are indispensable

0021-9991/02 $35.00

for attaining the full-scale solution for the Navier–Stokes equation. However, numerical simulation of incompressible and viscous flows can be a challenge. In many cases, computational difficulty stems from the inherently complex geometry and boundary conditions of the problem, which excludes the use of high-accuracy global methods. Complex geometry often induces singularities in a flow profile which creates numerical instabilities. A realistic 3D simulation for a complex geometric problem often requires millions of grid points and the amount of computations involved are formidable even for the most powerful supercomputer. Advances in computational algorithms is of prime importance for overcoming the above-mentioned difficulties.

A variety of numerical techniques have been developed in the last century. Generally speaking, computational methods which are currently employed in solving fluid flow problems can be classified into two categories: global methods and local methods. Global methods, such as spectral methods [1, 2], pseudospectral methods [3, 4], fast Fourier transform [5, 6], and differential quadrature [7], approximate a differentiation at one point by all grid points in the computational domain and thus can be highly accurate. For example, spectral methods converge exponentially with respect to mesh refinement for approximating an analytical function [4] and, thus, have the potential for being used in high-precision, highly demanding large-scale computations, such as the simulation of turbulence. Many global approaches have been successfully applied to the study of flow features in simple geometries, such as channels, pipes, eccentric cylinders, and so forth. However, global methods are well-known for their limitations in handling complex boundary conditions and irregular geometries. Indeed, for simulating the flow in complex geometries, local methods, such as finite differences [8, 9], finite elements [10–14], finite strips [15], and finite volumes [16], are the dominant approaches. Local methods utilize information at the nearest-neighboring grid points to approximate a differentiation at a point and, thus, are much more flexible in handling complex boundary conditions and irregular geometries. However, local methods converge slowly with respect to mesh refinement and are extremely expensive for achieving high precision. In cases such as combustion and turbulent flows, where high computational accuracy is desirable, global methods could be preferred. There are two ways to extend the applicability of global methods to complex boundaries. One approach is to divide the computational domain into a number of regular subdomains, and implement a spectral method within each of these subdomains. This multidomain approach is referred as spectral element method [17] and/or pseudospectral element method [18]. The objective of this approach is to maintain the spectral method's accuracy in the computations over irregular geometries [19]. The second approach involves a mapping of an irregular computational domain into a regular one, in which spectral methods can be implemented. One method to attain this mapping is through the solution of the Poisson equation for the new coordinates in terms of the old ones. This method was studied by many researchers [20, 21]. Significant progress has been made in both approaches. In particular, the spectral element approach has shown great promise for its application to complex geometries. However, development on this line is hindered by the fact that matching between different element domains leads to a devastative reduction in computational accuracy [17]. Consequently, the global accuracy is degraded by the poor approximation between element boundaries. How to achieve uniform convergence for the spectral element approximation remains a major issue of research. Recently, Yang *et al.* [22] proposed a domain-matching scheme which overlaps one grid point between the two neighboring spectral elements. As such, the grid sizes of all subdomains have to be the same and the overall accuracy is still quite low.

Recently, the discrete singular convolution (DSC) algorithm was proposed as a potential approach for the computerized realization of singular integrations [23, 24]. Mathematical foundation of the algorithm is the theory of distribution and wavelet analysis. Sequences of approximations to the singular kernels of Hilbert, Abel, and delta types were constructed. Applications to analytical signal processing, Radon transform, and surface interpolation are discussed. Numerical solutions to differential equations are formulated via singular kernels of the delta type. By appropriately choosing the DSC kernels, the DSC approach exhibits the global method's accuracy for integration and the local method's flexibility in handling complex geometries and boundary conditions. Many DSC kernels, such as (regularized) Shannon's delta kernel, (regularized) Dirichlet kernel, (regularized) Lagrange kernel, and (regularized) de la Vallée Poussin kernels, are constructed for a number of applications, such as numerical solution of the Fokker–Planck equation [23, 24] and the Schrödinger equation [25]. The DSC algorithm was also utilized for waveguide model analysis, electromagnetic wave propagation [26], and structural (plate and beam) analysis [27, 28] with excellent results. Most recently, the DSC algorithm was used to resolve a few numerically challenging problems. It was utilized to integrate the (nonlinear) sine–Gordon equation with the initial values close to a homoclinic orbit singularity [29], for which conventional local methods encounter great difficulties and numerically induced chaos was reported for such an integration [30]. Another difficult example, which could be resolved by using the DSC algorithm, is the integration of the (nonlinear) Cahn–Hilliard equation in a circular domain, which is challenging because of the fourth-order artificial singularity at the origin and the complex phase space geometry [31]. What is most relevant to the present work is the DSC solution for the Navier–Stokes equation. A DSC–successive overrelaxation (DSC–SOR) algorithm was developed for simulating the incompressible viscous flows with no-slip boundary condition for the driven cavity problem [32]. The DSC–SOR algorithm provides a potentially reliable approach for high-precision, large-scale computations. However, most of the previous use of the DSC algorithm was essentially on simple, regular domains.

The purpose of the present work is to develop a DSC–finite subdomain method (DSC–FSM). The previous DSC–SOR algorithm [32] is implemented inside each subdomain and a highly accurate DSC interpolation algorithm is employed for data transfer between any two neighboring subdomains. Although the present algorithm is constructed by using an idea similar to spectral elements or domain decomposition, the DSC algorithm is a distinct local approach with user-defined computational bandwidth and controllable accuracy.

This paper consists of four sections. Section 2 is devoted to the DSC–FSM. The DSC algorithm is briefly reviewed. The total computational domain is divided into a number of simple regular subdomains. The governing equations on each subdomain are described along with the solution procedure. A third-order Runge–Kutta scheme is employed for advancing the time. The governing equations are spatially discretized by using the DSC algorithm. A fractional-time-step and potential-function method (FTSPFM) [32] is adopted to overcome the difficulty which occurs in the treatment of the pressure field in incompressible flows. The iterative SOR solver is utilized for solving the resulting Neumann–Poisson equation. In Section 3, the validity and utility of the present DSC–FSM approach is explored for numerical simulation of incompressible flows. The approximation error and rate of convergence of the DSC–FSM method is examined by simulating the driven cavity flow at $\mathrm{Re} = 400, 5{,}000$, and 10,000. The flow over a backward-facing step and laminar flow past a square prism are numerically simulated to demonstrate the utility and robustness of the proposed method in handling more-complex problems. It is found that the present

numerical results agree well with the previous benchmark solutions and the experimental data available in the literature. Finally, conclusions are given in Section 4.

II. DISCRETE SINGULAR CONVOLUTION–FINITE SUBDOMAIN METHOD

The DSC–FSM is presented in this section. Detailed analysis and description is given in the following subsections.

A. Discrete Singular Convolution

For the sake of integrity and simplicity, the discrete singular convolution (DSC) algorithm is briefly described in this subsection. The reader is referred to the original papers [23, 24] for more details. The DSC algorithm concerns with computerized realization of evaluating mathematical distributions. Distributions are not well defined in the usual sense and may not have a value at all. Particular examples are kernels of the Hilbert and Abel types. These singular kernels are of crucial importance to a number of fields, such as electrodynamics, Radon transform, analytical function theory, linear response theory, and spectral property of correlation functions. For data (surface) interpolation and solving partial differential equations, singular kernels of the delta type are invoked. In the DSC algorithm, function $f(x)$ and its derivatives with respect to a coordinate at a grid point x are approximated by a linear sum of discrete values $\{f(x_k)\}$ in a narrow bandwidth $[x - x_W, x + x_W]$. This can be expressed as

$$f^{(q)}(x) \approx \sum_{k=-W}^{W} \delta_{\Delta,\sigma}^{(q)}(x - x_k) f(x_k), \tag{1}$$

where superscript q ($q = 0, 1, 2, \ldots$) denotes the qth-order derivative with respect to x. The $\{x_k\}$ is a set of discrete sampling points centered around the point x. Here σ is a regularization parameter, Δ is the grid spacing, and $2W + 1$ is the computational bandwidth, which is usually smaller than the size of the computational domain.

In Eq. (1), $\delta_{\Delta,\sigma}(x)$ is a convolution kernel that is an approximation to the delta distribution. For band-limited functions, the delta distribution can be replaced by an ideal low-pass filter; hence, many wavelet scaling functions can be used as the DSC convolution kernels. One interesting example is to regularize Shannon's wavelet scaling function,

$$\delta_{\Delta,\sigma}(x - x_k) = \frac{\sin \frac{\pi}{\Delta}(x - x_k)}{\frac{\pi}{\Delta}(x - x_k)} \exp\left(-\frac{(x - x_k)^2}{2\sigma^2}\right), \quad \sigma > 0, \tag{2}$$

where σ determines the width of the Gaussian envelop and is often varied in association with the grid spacing, i.e., $\sigma = r\Delta$, where r is a parameter chosen in computations. The expression in Eq. (2) is often referred as regularized Shannon's delta kernel. Note that the use of the Gaussian regularizer can extend the domain of applicability of the delta kernels to tempered distributions and even to exponentially growing functions [34]. The expression of Eq. (1) provides extremely high computational efficiency both on and off a grid. In fact, with an appropriate σ, it can provide exact results when the sampling points are extended to a set of infinite points for certain band-limited L^2 functions. By appropriately choosing W, r, and Δ, the resulting approximation matrix for interpolation and solving differential equations has a banded structure, which gives the DSC algorithm optimal accuracy and efficiency for a variety of numerical computations.

It should be pointed out that although the regularized Shannon's delta kernel is used to illustrate the DSC approximation of the delta distribution here, there are many other DSC kernels that perform equally well, as shown elsewhere [23, 26, 29]. The grid used in Eq. (1) is uniform because only a single grid spacing is prescribed. In computations, Eq. (1) is very efficient since just one kernel is required for the whole computational domain $[a, b]$ for given Δ and r. We refer to this kernel as being translationally invariant. It is noted that to maintain the kernel property of translation invariance near a computational boundary, the functions $f(x_k)$ have to be located outside the computational domain $[a, b]$, where their values are usually undefined. Therefore, it is necessary to create fictitious domains outside the computational boundaries. In the DSC algorithm, function values at these fictitious domains are generated according to the boundary condition and the physical behavior of the solution at the boundaries. For example, in Dirichlet boundary conditions, such $f(x_k)$ can be taken to be $f(a)$ or $f(b)$; in periodic boundary conditions, such $f(x_k)$ may be obtained by a periodic extension from their corresponding values inside the computational domain $[a, b]$; and in Neumann boundary conditions, such $f(x_k)$ may be determined by $f'(a)$ (or $f'(b)$).

When the regularized Shannon's delta kernel is used, the detailed expressions for $\delta^{(q)}_{\Delta,\sigma}(x)$ can be analytically given by differentiations,

$$\delta^{(q)}_{\Delta,\sigma}(x) = \frac{d^q}{dx^q}\left[\frac{\sin\frac{\pi}{\Delta}x}{\frac{\pi}{\Delta}x}\exp\left(-\frac{x^2}{2\sigma^2}\right)\right]. \tag{3}$$

Once the value of r is chosen, the coefficients $\delta^{(0)}_{\Delta,\sigma}(x)$, $\delta^{(1)}_{\Delta,\sigma}(x)$, and $\delta^{(2)}_{\Delta,\sigma}(x)$ depend only on the grid spacing Δ. Therefore, when the grid spacing is prescribed, the coefficients need to be computed only once and can be used during the entire computation.

B. Governing Equations and Method of Solution

The Navier–Stokes equations, which govern the incompressible, viscous flow in two-dimensions are

$$D(U) = 0, \tag{4}$$

$$\frac{\partial U}{\partial t} = F(U) - \nabla p, \tag{5}$$

where

$$D(U) = \frac{\partial u}{\partial x} + \frac{\partial v}{\partial y}, \tag{6}$$

$$F(U) = [f, g]^T, \quad U = [u, v]^T, \quad \nabla p = \left[\frac{\partial p}{\partial x}, \frac{\partial p}{\partial y}\right]^T, \tag{7}$$

$$\begin{aligned} f &= \frac{1}{\mathrm{Re}}\left(\frac{\partial^2 u}{\partial x^2} + \frac{\partial^2 u}{\partial y^2}\right) - \left(u\frac{\partial u}{\partial x} + v\frac{\partial u}{\partial y}\right), \\ g &= \frac{1}{\mathrm{Re}}\left(\frac{\partial^2 v}{\partial x^2} + \frac{\partial^2 v}{\partial y^2}\right) - \left(u\frac{\partial v}{\partial x} + v\frac{\partial v}{\partial y}\right). \end{aligned} \tag{8}$$

Here, the velocity components in the x- and y-directions are represented by u and v, respectively, and p the pressure, t the time, ρ the fluid density, and the Reynolds number $\mathrm{Re} = U_0 L/\nu$, in which ν is the kinematic viscosity of the fluid.

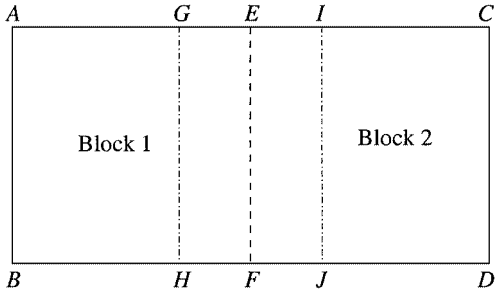

FIG. 1. Subdomain division with interfaces and fictitious overlapping zones.

For incompressible flows, there is no coupling between the continuity and momentum equations (4) and (5). To overcome the difficulty in solving these equations, a well-known approach is to derive the Poisson equation for pressure from the incompressible condition, Eq. (4). Many specially designed schemes have been developed [35–40]. In this work, we adopt a fractional-time-step and potential-function method (FTSPFM), which is a variant of the marker and cell (MAC) method [39] for solving the governing Eqs. (4) and (5). In the FTSPFM approach, an intermediate velocity field and a potential function are employed to update the values of the velocity and pressure fields at a new time step [32]. The present explicit scheme holds special appeal for extending it to complex geometries. The choice of an implicit or a semi-implicit version is, in general, constrained by the large-scale memory requirements and the inevitable matrix inversion procedure which consumes a huge CPU time. Nevertheless, an implicit scheme was implemented in conjunction with a simply connected square domain [27].

The total computational domain is divided into a number of simple subblocks. A uniform grid in both x- and y-directions is employed within each subdomain. The present treatment of block interfaces is distinct from the conventional approaches, due to the existence of fictitious domains. Due to the nature of the support envelope employed in DSC, it requires fictitious overlapping subdomains. This relation between subdomains is illustrated in Fig. 1. Block *ABDC* is divided into two subdomains, *ABFE* and *EFDC*. The dashed-line EF is the common line connecting block *ABFE* and block *EFDC*. The area of *GHFE* is a fictitious domain of *EFDC* and a *fictitious overlapping zone* for subdomain *ABFE*. Similarly, the area of *EFJI* is a fictitious domain of *ABFE* and a fictitious overlapping zone for subdomain *EFDC*. The size of fictitious overlapping zones is determined by the computational bandwidth W chosen in the DSC algorithm. Hence, it is very flexible and can be adjusted to the size of the overlapping zones to meet the accuracy requirement of different problems by changing the value of the computational bandwidth W. The DSC algorithm is indeed employed for both interpolation and information exchange among neighboring subdomains.

All spatial derivatives in Eqs. (4) and (5) are discretized by using the DSC algorithm. In each subdomain, the momentum equation in the horizontal direction is written at point $(i + \frac{1}{2}, j)$, the momentum equation in the vertical direction is written at point $(i, j + \frac{1}{2})$, and the pressure is written at point (i, j). The staggered grid system is shown in Fig. 2. The continuity equation is approximated at point (i, j). Therefore, the discretized forms of Eqs. (6)–(8) can then be expressed as

$$D_h(U) = \sum_{k=-W}^{W} \delta^{(1)}_{\Delta,\sigma}(k\Delta x_N) u_{i+k,j} + \sum_{k=-W}^{W} \delta^{(1)}_{\Delta,\sigma}(k\Delta y_N) v_{i,j+k}, \tag{9}$$

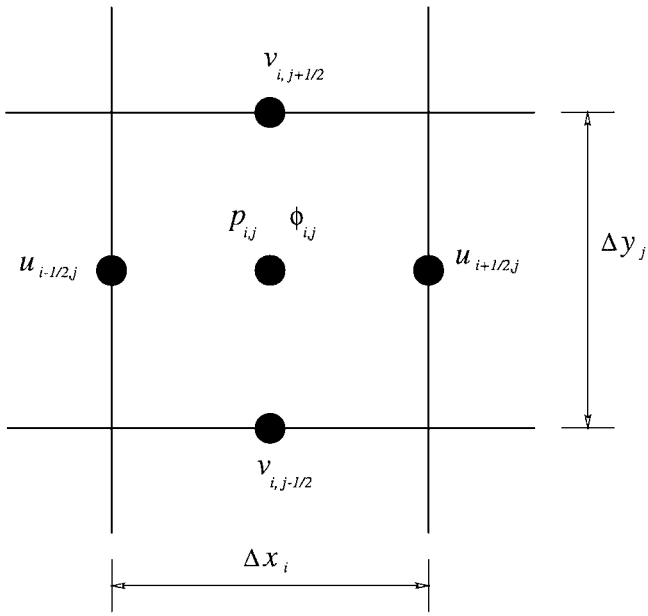

FIG. 2. The staggered grid system.

$$\nabla_h p = \left[\sum_{k=-W}^{W} \delta^{(1)}_{\Delta,\sigma}(k\Delta x_N) p_{i+k,j}, \sum_{k=-W}^{W} \delta^{(1)}_{\Delta,\sigma}(k\Delta y_N) p_{i,j+k} \right]^T, \tag{10}$$

$$f_h = \frac{1}{\mathrm{Re}} \left[\sum_{k=-W}^{W} \delta^{(2)}_{\Delta,\sigma}(k\Delta x_N) u_{i+\frac{1}{2}+k,j} + \sum_{k=-W}^{W} \delta^{(2)}_{\Delta,\sigma}(k\Delta y_N) u_{i+\frac{1}{2},j+k} \right] - \left[u_{i+\frac{1}{2},j} \sum_{k=-W}^{W} \delta^{(1)}_{\Delta,\sigma}(k\Delta x_N)\left(u_{i+\frac{1}{2}+k,j}\right) + v_{i+\frac{1}{2},j} \sum_{k=-W}^{W} \delta^{(1)}_{\Delta,\sigma}(k\Delta y_N)\left(u_{i+\frac{1}{2},j+k}\right) \right], \tag{11}$$

$$g_h = \frac{1}{\mathrm{Re}} \left[\sum_{k=-W}^{W} \delta^{(2)}_{\Delta,\sigma}(k\Delta x_N) v_{i+k,j+\frac{1}{2}} + \sum_{k=-W}^{W} \delta^{(2)}_{\Delta,\sigma}(k\Delta y_N) v_{i,j+\frac{1}{2}+k} \right] - \left[u_{i,j+\frac{1}{2}} \sum_{k=-W}^{W} \delta^{(1)}_{\Delta,\sigma}(k\Delta x_N)\left(v_{i+k,j+\frac{1}{2}}\right) + v_{i,j+\frac{1}{2}} \sum_{k=-W}^{W} \delta^{(1)}_{\Delta,\sigma}(k\Delta y_N)\left(v_{i,j+\frac{1}{2}+k}\right) \right], \tag{12}$$

$$F_h(U) = [f_h, g_h]^T, \tag{13}$$

where $\delta^{(1)}_{\Delta,\sigma}$ and $\delta^{(2)}_{\Delta,\sigma}$ are coefficients of the regularized Shannon's delta kernel, given in Eq. (3). The spatial discretization labels (subscripts) on the left hand sides are omitted for simplicity. Here, Δx_N and Δy_N denote the grid spacings in the x- and y-directions, respectively, for the Nth computational block. By substituting Eqs. (9)–(13) into Eqs. (4) and (5), the following semidiscretized approximation for Eqs. (4) and (5) is obtained:

$$D_h(U) = 0, \tag{14}$$

$$\frac{dU}{dt} = F_h(U) - \nabla_h p. \tag{15}$$

A third-order Runge–Kutta (R–K) scheme is employed for the temporal discretization. In this scheme, the ordinary differential equation (15) can be solved by

$$U^{(1)} = \alpha_1 U^n + \beta_1 \left[\Delta t \left(F_h(U^n) - \nabla_h p^{(1)}\right)\right], \tag{16}$$

$$U^{(2)} = \alpha_2 U^n + \beta_2 \left[U^{(1)} + \Delta t \left(F_h\left(U^{(1)}\right) - \nabla_h p^{(2)}\right)\right], \tag{17}$$

$$U^{n+1} = \alpha_3 U^n + \beta_3 \left[U^{(2)} + \Delta t \left(F_h\left(U^{(2)}\right) - \nabla_h p^{n+1}\right)\right], \tag{18}$$

where $(\alpha_1, \alpha_2, \alpha_3) = (1, 3/4, 1/3)$ and $(\beta_1, \beta_2, \beta_3) = (1, 1/4, 2/3)$. Here, Δt is the time increment in each iteration. The U^n and p^n are the velocity and pressure at time t_n, respectively. The $U^{(1)}$, $p^{(1)}$ and $U^{(2)}$, $p^{(2)}$ are their corresponding first- and second-step values, while U^{n+1} and p^{n+1} are the velocity and pressure at time t_{n+1}, respectively.

The integration stability of the explicit scheme is limited by the the Courant–Friedrich–Lewy (CFL) condition [41], which is given as

$$\max(\Delta t) \leq \min\left(\frac{4}{\mathrm{Re}(|u| + |v|)^2}, \frac{\mathrm{Re}((\Delta x_N)^2 + (\Delta y_N)^2)}{4}\right). \tag{19}$$

A fractional-time-step and potential-function method (FTSPFM) [32] associated with Eqs. (14) and (16)–(18) is employed to update the values of the velocity and pressure fields at a new time step, while an iterative SOR solver is utilized for solving the resulting Neumann–Poisson equation. The details of the discretized expressions for the FTSPFM and elaborate details of the numerical solution procedure are available in Refs. [32, 33].

III. RESULTS AND DISCUSSION

In this section, we examine the validity and explore the utility of the DSC–FSM approach for the numerical simulation of incompressible viscous flows. As a precursor, the 2D incompressible Navier–Stokes equations (4) and (5) in a square domain with periodic boundary conditions, the Taylor problem, are solved to validate the proposed method. The exact solution is available. The L_1 and L_∞ errors and numerical orders are compiled in Table I for $\mathrm{Re} = \infty$. Excellent accuracy is achieved with small mesh sizes. Some numerical orders are as high as 17.7, indicating that the proposed approach is extremely accurate. More details about solving this problem can be found in Ref. [27].

Further, three benchmark problems, viz., flow in a driven cavity, flow over a backward-facing step, and flow past a square prism, are chosen for the investigation. Although the first two problems have a simply connected geometry, they depict rich and complex fluid flow patterns. Also, the accurate simulation of the complex spatiotemporal dynamics in the third problem constitutes a severe test for the new computational scheme. In these simulations, the computational bandwidth and regularization parameter are chosen as $W = 16$ and $r = 2.85$, respectively. Indeed, it is possible to achieve even higher computational accuracy for a given fluid flow problem, by choosing a larger computational bandwidth and its corresponding value of r. The relation between the numerical accuracy

TABLE I
Errors and Numerical Orders for the Taylor Problem

N	Time	L_1 error	L_1 order	L_∞ error	L_∞ order
8	1.0	1.52 (−4)	—	5.13 (−5)	—
	2.0	2.17 (−4)	—	7.13 (−5)	—
16	1.0	6.76 (−10)	17.78	6.82 (−10)	16.2
	2.0	9.68 (−10)	17.77	8.81 (−10)	16.3
32	1.0	2.03 (−14)	15.02	1.45 (−14)	15.52
	2.0	4.05 (−14)	14.54	2.31 (−14)	15.22

Note. N refers to the number of grid points in each dimension.

and the DSC parameters was explored for the incompressible Euler flow problem [24]. The overrelaxation factor is set to $\omega = 1.28$. It is quite efficient to set the convergence constant as small as $\varepsilon = 10^{-6}$. All computations were carried out on DEC/Compaq workstations.

A. Lid-Driven Cavity Flow: A Numerical Test

Flow in a lid-driven cavity is among the well-established benchmark test problems used to check the reliability of new computational schemes. The wide popularity of this test problem can be attributed to the following: (i) a complete lack of ambiguity in enforcing the boundary conditions; (ii) a fixed fluid flow domain of interest even with an increase in the Reynolds number (Re); and (iii) the existence of a variety of the fluid flow phenomena that occur in incompressible flows, viz., eddies, secondary flows, complex 3D flow patterns. It is indeed a challenge to any potential numerical method to simulate the entire spectrum of these fluid flow features (which vary with the Reynolds number). Thus, the problem of flow in a driven cavity offers an ideal framework in which meaningful and detailed comparisons can be made between the results obtained from experiment, theory, and computation [42]. The availability of a vast amount of literature [43–46] is a testimony to this. Therefore, it is quite natural to choose this problem for an extensive validation of the present DSC–FSM approach. The flow domain of interest is a unit square with the upper horizontal lid moving with a uniform velocity ($u = 1.0$, $v = 0.0$). A no-slip boundary condition ($u = v = 0.0$) is applied on all the static walls. The velocity at both the left and right top corners of the domain is fixed as zero, to avoid any mass/momentum flow through the first two vertical nodes. The value of the potential function is set to a fixed value (zero) at the midpoint of the bottom side to ensure a unique solution for pressure.

Error accumulation is an inevitable by-product in the process of transforming the (continuous) governing partial differential equations over a domain into a set of coupled algebraic equations to obtain a numerical solution at discrete grid points. These errors could be due to truncation, round off, approximation, interpolation, relaxation parameter, and so forth. However, these errors should not be allowed to be magnified during the course of the numerical simulation. Thus, it becomes the duty of the numerical fluid flow analyst to ensure that the accuracy of numerical results is within an acceptable error bound. Several procedures can be built to reduce this error in a systematic fashion.

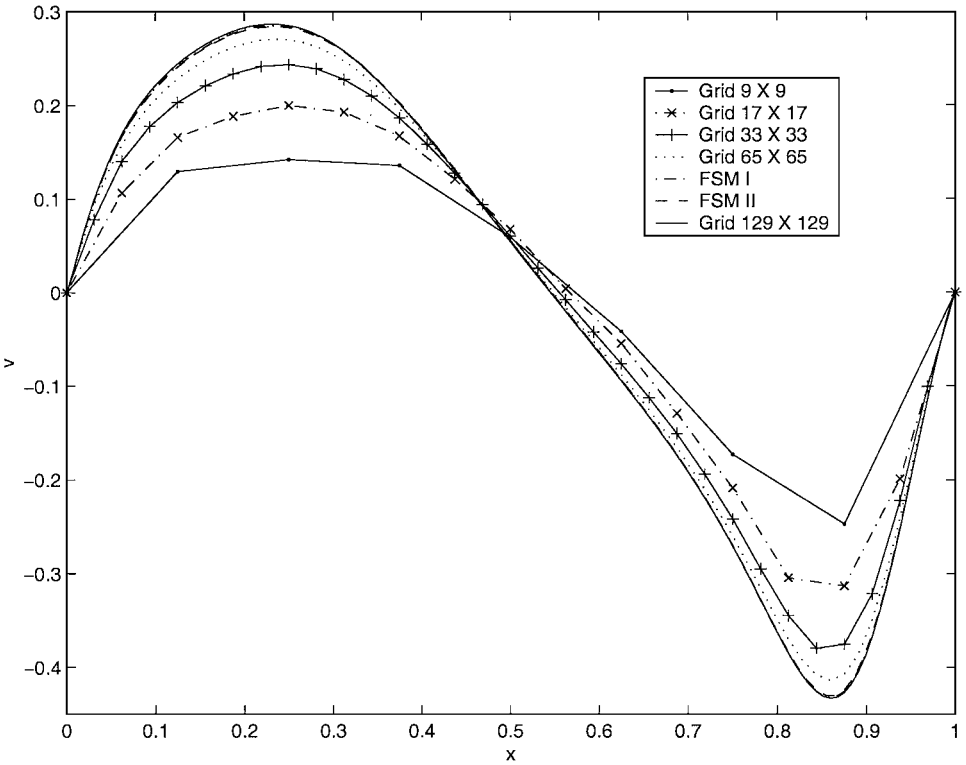

FIG. 3. The steady state vertical velocity in a lid-driven cavity at midheight (Re = 400).

Grid independence. It is important to prove that the numerical solution that was obtained from the present approach is grid independent. To this end, we employ a series of mesh systems to test the DSC–FSM approach. The following uniform mesh systems were employed: 9×9, 17×17, 33×33, 65×65, and 129×129. Furthermore, two finite subdomain mesh systems, FSM I and FSM II, were designed with four quadrants. FSM I has a 65×65 grid in the first and third quadrants, while FSM II has a 129×129 grid. In the second and fourth quadrants, FSM I has a 129×129 grid, while FSM II has a 65×65 grid. The performance of DSC–FSM on the above-mentioned grid systems is summarized in terms of predicted velocity distribution for $\mathrm{Re} = 400$. Here, the vertical velocity is shown in Fig. 3 against the abscissa at midheight ($y = 0.5$). The variation between the results obtained by different grid systems beyond 65×65 grid points is indiscernible. Even the two finite subdomain mesh systems have shown very close correspondence with a 129×129 grid. Thus, the solution obtained by DSC–FSM has a grid-independent character beyond a mesh size of 65×65 grid points.

Convergence. It is customary to look at the rate of convergence for different time steps adopted in a numerical simulation. The convergence history in terms of the residuals ($Res(U)$) shown in Fig. 4 refers to different mesh systems used. The $Res(U)$ is defined as follows:

$$Res(u) = \max_{i,j}\left[\frac{\left(u^n_{i,j} - u^{n-1}_{i,j}\right)}{u^n_{i,j}}\right]. \tag{20}$$

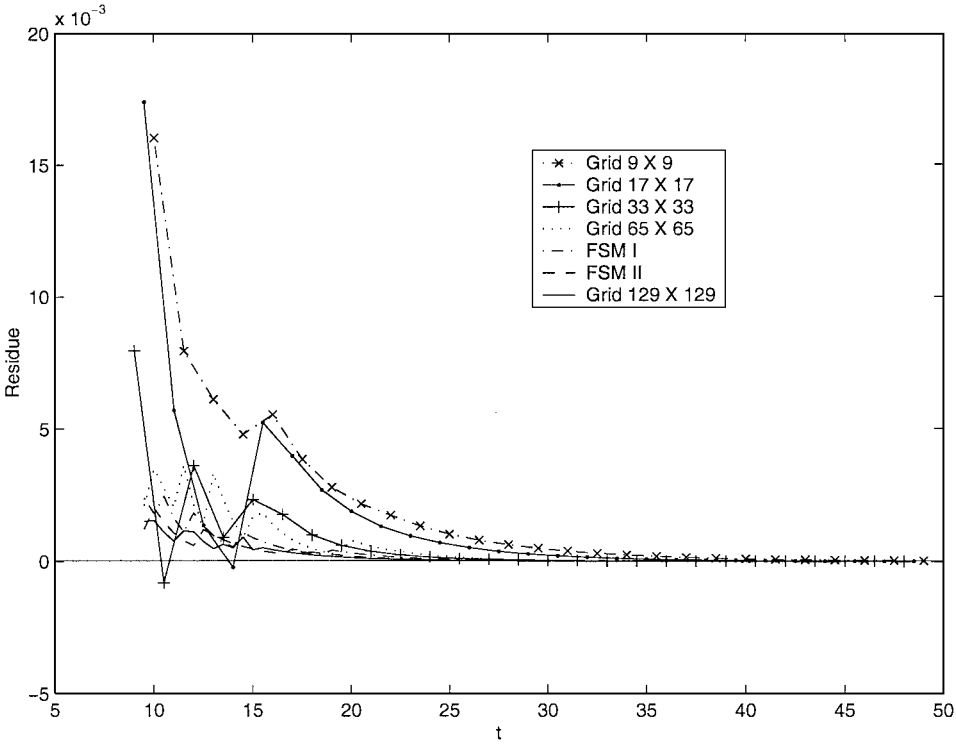

FIG. 4. Comparison of the rate of convergence for the lid-driven cavity flow (Re = 400).

In the above equation, the subscript (i, j) refers to the grid point, and n and $n - 1$ refer to the current and previous time steps, respectively. We can see in Fig. 4 that results on a fine mesh exhibit a better convergence history than those on a coarse mesh.

A comparison exercise. A quantitative comparison with the previous benchmark results obtained by Ghia *et al.* [44] is presented in Tables II and III for the numerical values along the midsection of the cavity. The results from the mesh system 129×129, from FSM I and FSM II, as well as that obtained by Ghia *et al.* [44] are listed. It is noted that all three DSC-based computational results are highly consistent with each other. Therefore, the results obtained by using the present domain decomposition approach are as reliable as those obtained by using a single domain. There are some minor differences between the DSC results and those of Ghia *et al.* [44]. However, such minor differences among the results obtained from different numerical schemes are well within the acceptable limits.

Streamlines and vorticity contours are depicted in Figs. 5a and 5b for Re = 400. To resolve the thin shear layers more prominently, the simulations were performed at very the high Reynolds numbers of 5,000 and 10,000. Corresponding streamline visuals are presented in Fig. 6. In the streamline plot, for Re = 400, there is one dominant primary circulation, apart from two secondary eddies on the two bottom corners of the cavity. At higher Reynolds numbers, another secondary eddy emerges at the top left corner of the cavity. The streamfunction and vorticity values labeled on the plot are in excellent agreement with the earlier investigations [43–46]. Table IV summarizes the minimum value of streamfunction obtained from different mesh systems. These values are in good conformity with those obtained by the earlier investigations.

TABLE II
Comparison of the u-Velocity Profile at $x = 0.5$ through the Geometric Center of the Cavity

y	Ghia *et al.* [44]	129×129	FSM I	FSM II
0.0000	0.00000	0.0000000	0.0000000	0.0000000
0.0547	−0.08186	−0.0786065	−0.0786185	−0.0786129
0.0625	−0.09266	−0.0890649	−0.0890786	−0.0890722
0.0703	−0.10338	−0.0994432	−0.0994584	−0.0994465
0.1016	−0.14612	−0.1408370	−0.1408582	−0.1408399
0.1719	−0.24299	−0.2351602	−0.2351944	−0.2351480
0.2813	−0.32726	−0.3200354	−0.3200696	−0.3199771
0.4531	−0.17119	−0.1691814	−0.1691909	−0.1691994
0.5000	−0.11477	−0.1133524	−0.1133480	−0.1132946
0.6172	0.02135	0.0212599	0.0212582	0.0212557
0.7344	0.16256	0.1601330	0.1601422	0.1601131
0.8516	0.29093	0.2859086	0.2859320	0.2858630
0.9531	0.55892	0.5609661	0.5610127	0.5608601
0.9609	0.61756	0.6204921	0.6205649	0.6204080
0.9688	0.68439	0.6880549	0.6881639	0.6880108
0.9766	0.75837	0.7625521	0.7627000	0.7625694
1.0000	1.00000	1.0000000	1.0000000	1.0000000

B. Flow over a Backward-Facing Step

Having established our confidence in the utility of the DSC–FSM scheme for the simulation of incompressible flows in a simple square geometry, we consider a more complex problem—the flow over a backward-facing step. This problem has several attractive

TABLE III
Comparison of the v-Velocity Profile at $y = 0.5$ through the Geometric Center of the Cavity

x	Ghia *et al.* [44]	129×129	FSM I	FSM II
0.0000	0.00000	0.0000000	0.0000000	0.0000000
0.0625	0.18360	0.1771959	0.1773318	0.1773084
0.0703	0.19713	0.1906195	0.1907233	0.1906780
0.0781	0.20920	0.2025996	0.2026822	0.2026183
0.0938	0.22965	0.2229257	0.2229858	0.2229127
0.1563	0.28124	0.2740663	0.2741116	0.2740313
0.2266	0.30203	0.2950392	0.2950785	0.2950257
0.2344	0.30174	0.2948710	0.2949092	0.2948241
0.5000	0.05186	0.0530158	0.0530098	0.0530301
0.8047	−0.38598	−0.3784859	−0.3785206	−0.3784538
0.8594	−0.44993	−0.4431324	−0.4431778	−0.4430990
0.9063	−0.23827	−0.3782805	−0.3783378	−0.3782805
0.9453	−0.22847	−0.2263186	−0.2265009	−0.2265056
0.9531	−0.19254	−0.1906588	−0.1909120	−0.1909427
0.9609	−0.15663	−0.1548964	−0.1552420	−0.1553124
0.9688	−0.12146	−0.119740	−0.1201912	−0.1203259
1.0000	0.00000	0.0000000	0.0000000	0.0000000

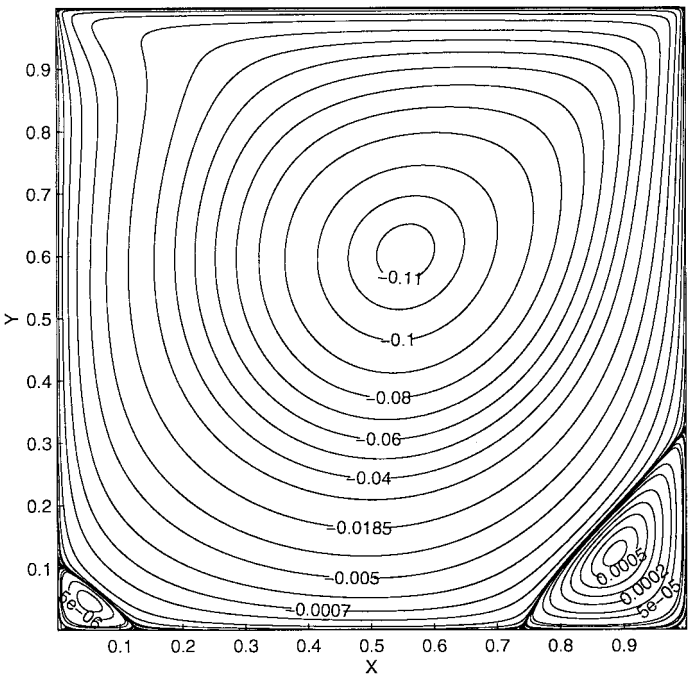

(a) streamline contours

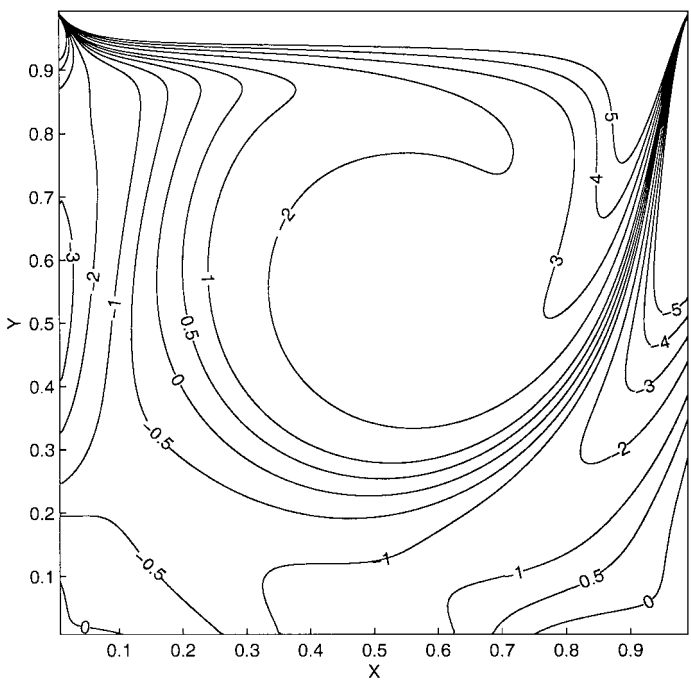

(b) vorticity contours

FIG. 5. Contour plots for the lid-driven cavity flow (Re = 400). (a) Streamline contours; (b) vorticity contours.

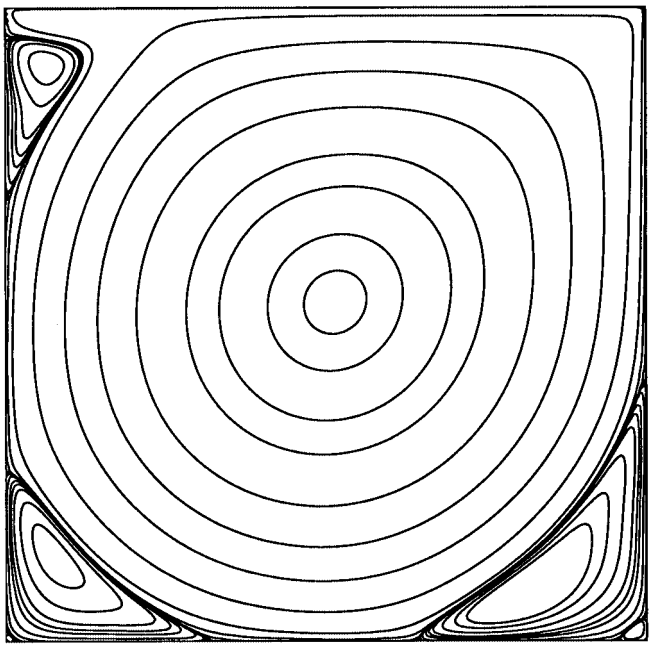

(a) Re=5000

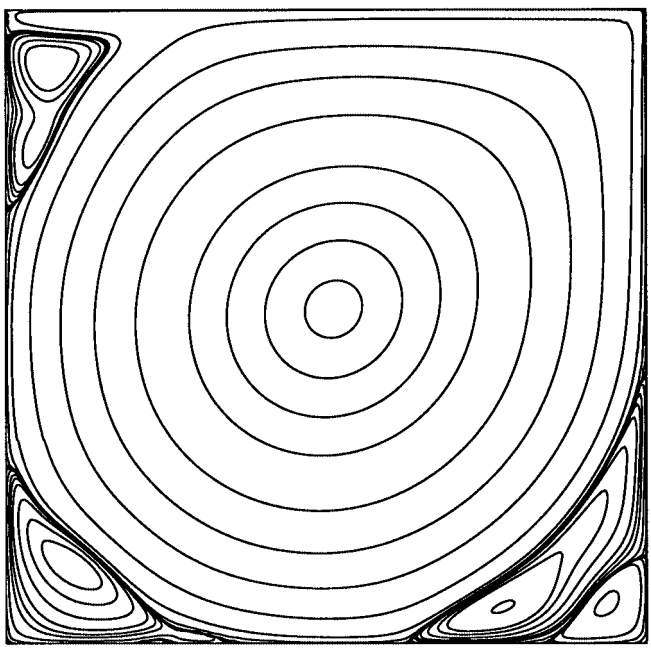

(b) Re = 10000

FIG. 6. Streamline visuals at high Reynolds numbers: (a) Re = 5,000; (b) Re = 10,000.

features, such as flow separation and recirculation zone. Indeed, the problem resembles a two-dimensional plane version of sudden expansion in a pipe. To start with, the problem is defined, then followed by convergence study and a discussion on the results obtained.

TABLE IV
Comparison of the Minimum Streamfunction Value for Re = 400

Mesh or reference	$\psi_{\min}$
9×9	−0.054083
17×17	−0.078159
33×33	−0.093478
65×65	−0.115421
129×129	−0.114010
FSM I	−0.113985
FSM II	−0.114037
Ref. [45]	−0.118
Ref. [46]	−0.108
Ref. [43]	−0.114
Ref. [44]	−0.113909

A backward-facing step is classified according to the expansion ratio of the channel, which is defined as $D/(D - H)$. Here, D refers to the channel height on the downstream side of the step and H is the height of the channel. An expansion ratio of 2 : 1 is chosen to validate the results of the present investigation with the available experimental results of Ref. [47] and the numerical results of Refs. [48, 49]. Channel lengths on the upstream and downstream sides of the step are denoted W_I and W_E, which are chosen as 4 and 18, respectively. The Reynolds number of the flow is defined as $\mathrm{Re} = HV_\infty/\nu$, where V_∞ is the velocity at the inlet and ν is the kinematic viscosity of the fluid. Simulations are performed over the Reynolds number range of 25–400. It should be pointed out that no experiment is exactly two dimensional for Re > 200. Furthermore, due to the loss of steadiness, three-dimensional features become dominant when the Reynolds number reaches a value of 400. Hence, our investigation is confined to $\mathrm{Re} \leq 400$.

The imposed boundary conditions are as follows.

- Channel inlet: A uniform velocity profile, which is given as

$$U = [u(0, y, t), v(0, y, t)]^T = [1, 0]^T. \tag{21}$$

- Channel walls: A no-slip boundary condition, which is given as

$$U = [u, v]^T = [0, 0]^T. \tag{22}$$

- Channel exit boundary ($x = W_I + W_E$): A Neumann boundary condition, which is given as

$$\frac{\partial U}{\partial x} = \left[\frac{\partial u}{\partial x}, \frac{\partial v}{\partial x}\right]^T = [0, 0]^T. \tag{23}$$

Although the computational domain appears simple, as shown in Fig. 7, it contains all the essential features of a complex geometry. In the present approach, the entire computational domain is divided into three regular subdomains. Block 2 covers a subdomain with a special

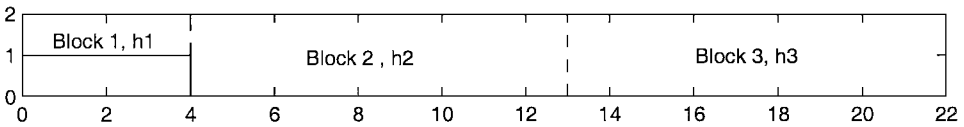

FIG. 7. The computational domain and finite subdomains for flow over a backward-facing step.

zone of interest with distinct fluid flow patterns. Such a division allows a judicious and controllable grid size in each block. The same uniform mesh is used in blocks 1 and 3 ($\Delta x = \Delta y = h1 = h3$), while block 2 has a mesh with $\Delta x = \Delta y = h2$. The two types of finite subdomain mesh (FSM) systems employed are FSM III ($h1 = 1/32, h2 = 1/48$) and FSM IV ($h1 = 1/48, h2 = 1/64$). Thus, the two mesh systems will enable a check on the grid sensitivity of the present simulations.

In order to obtain a unique solution, the potential function $\phi^{(k)}$ ($k = 1, 2, 3$) at one of the grid points ($x = 2$, $y = 1$) is fixed as zero at each step of the third-order Runge–Kutta scheme. The velocity and pressure initial conditions are set to zero inside each block of the domain. In order to obtain a smoother temporal evolution for the fluid flow features, the u-velocity value at the inlet boundary is increased from zero at $t = 0.0$ to a constant value of 1.0 over 200 time steps.

To verify the convergence behavior of the present DSC–FSM simulations over the mesh systems chosen, velocity residual error norm in L_2 is defined as

$$e(t) = \left|\left|U_{i,j}^{n} - U_{i,j}^{n-1}\right|\right|_{l_2} = \sqrt{\sum_{\text{Block}=1}^{3} \sum_{i,j} \left(\left|U_{i,j}^{n}\right| - \left|U_{i,j}^{n-1}\right|\right)^2} \tag{24}$$

and

$$|U_{i,j}| = \sqrt{(u_{i,j})^2 + (v_{i,j})^2}, \tag{25}$$

where the superscripts n and $n - 1$ denotes the current time step and the previous time step, respectively. The subscript (i, j) refers to its corresponding grid point. The convergence history for $e(t)$ is plotted in Fig. 8 for different Reynolds numbers with the mesh system FSM III ($h1 = 1/32, h2 = 1/48$). As can be observed, the solution reaches steady state within a short time for Re = 25. However, it takes a longer time to reach steady state at higher Reynolds numbers.

Fluid flow features. Streamlines which exemplify the basic fluid flow features in the channel are presented in Fig. 9 over the Re range of 25–400. Flow separation occurs when the fluid comes in contact with the upper corner of the step, and a dominant zone of recirculation is formed on the downstream. As can be observed, the size of this recirculation zone grows with an increase in the Reynolds number. The length of the recirculation bubble x_R is the single most important parameter of interest in these simulations. It is the distance between the step vertical wall (the point of separation) and the point of reattachment. The value of x_R can be determined in several ways. It can be measured from the streamline visuals in Fig. 9. However, to obtain the value in a precise fashion, the value of x, where stream function $\psi(x, 0) = 0$, is identified. The distance between this value of x and the step refers to the length of reattachment. The variation of reattachment length as a function of

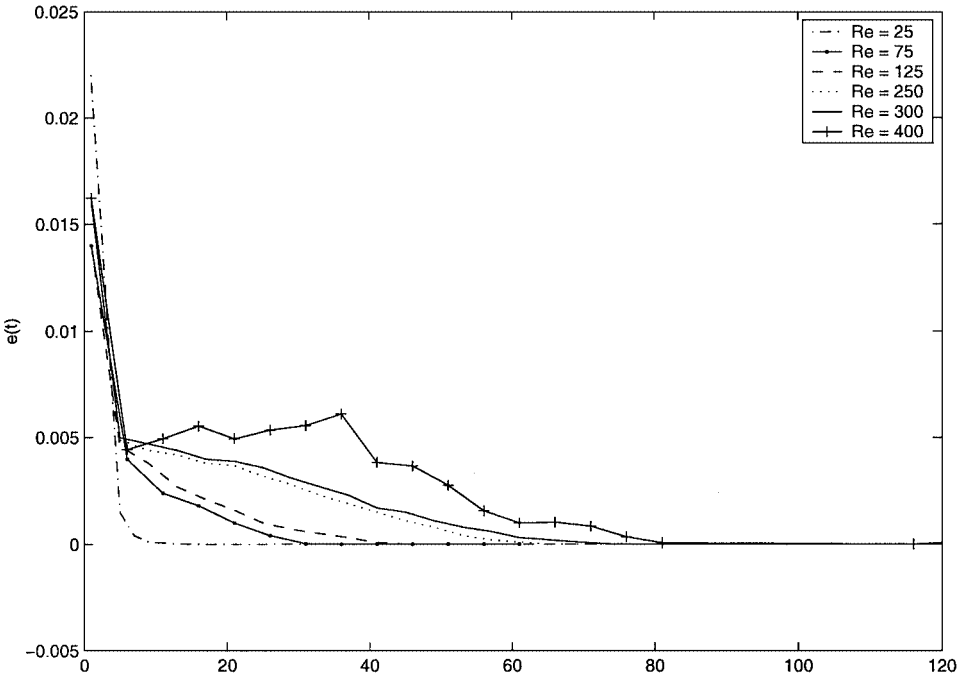

FIG. 8. The time history of $e(t)$ for flow over a backward-facing step at different Reynolds numbers obtained by using FSM III ($h1 = 1/32$, $h2 = 1/48$).

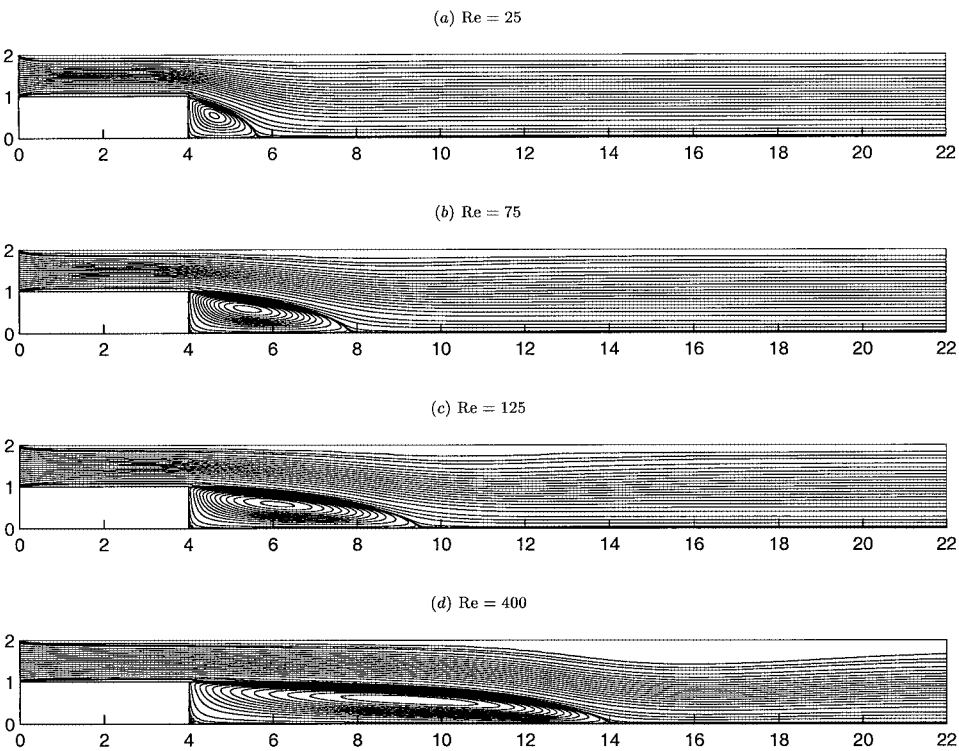

FIG. 9. The steady state streamline contours of flow over a backward-facing step obtained by using FSM III ($h1 = 1/32$, $h2 = 1/48$). (a) Re = 25, (b) Re = 75, (c) Re = 125, (d) Re = 400.

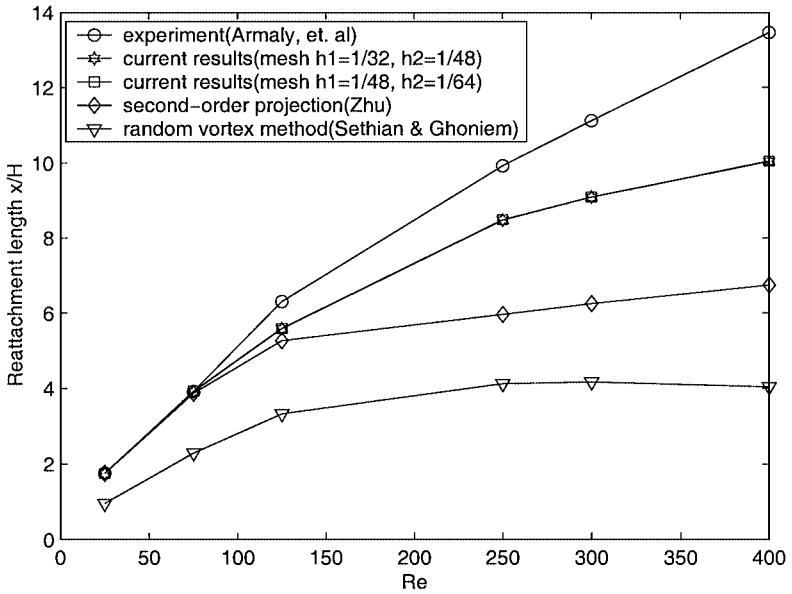

FIG. 10. The dependence of reattachment length x_R (x/H) for the flow over a backward-facing step at Reynolds numbers $25 \leq \mathrm{Re} \leq 400$.

the Reynolds number is plotted in Fig. 10 for $25 \leq \mathrm{Re} \leq 400$. Apart from the experimental values of Armaly *et al.* [47], numerical results from Refs. [48, 49] are also plotted. The detailed values are listed in Table V. Although none of the numerical predictions are closer to the experimental values, the DSC–FSM results are more encouraging than those of Zhu [49] and Sethian and Ghoneim [48]. As pointed out earlier, the disagreement between the numerical and experimental predictions is attributed to the three-dimensionality effects associated with the latter. The three-dimensionality factor becomes more and more obvious and important as Reynolds number increases.

C. Flow Past a Square Prism

The flow past a square prism is complex due to the multiply connected nature of the computational domain. The complex fluid flow patterns that evolve with time adds to this

TABLE V
Reattachment Length (x_R) for the Flow over a Backward-Facing Step

	Re					
	25	75	125	250	300	400
Experimental (Ref. [47])	1.7550	3.9208	6.3083	9.9167	11.1167	13.4583
Present study (SFM III)	1.7529	3.9176	5.5882	8.4706	9.0824	10.0353
Present study (SFM IV)	1.7531	3.9281	5.5907	8.4788	9.0891	10.0418
Numerical (Ref. [49])	1.7500	3.8750	5.2667	5.9583	6.2500	6.7500
Numerical (Ref. [48])	0.9583	2.2917	3.3333	4.1250	4.1667	4.0417

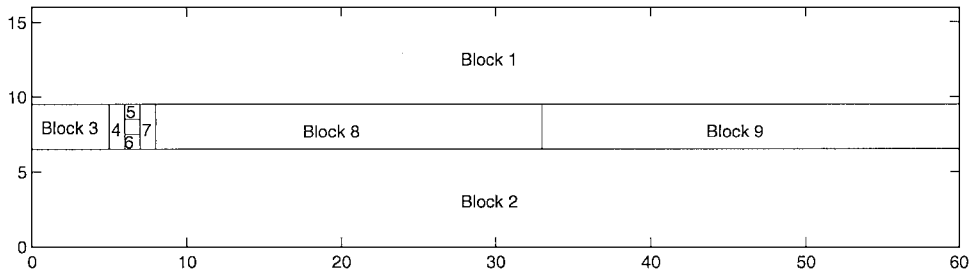

FIG. 11. The geometry of the computational domain and finite subdomains for flow past a square prism.

complexity. Thus, simulation of this problem becomes a severe test case to check the robustness and reliability of the DSC–FSM approach. For flow past a circular cylinder, the onset of 3D wake structures occurs at Re $\approx$ 180 [56]. However, for the square cylinder, no such clear value is found in the literature. It is believed that because such a value will be around Re $\leq$ 300, transition to turbulence takes place in the free shear layers [57]. Beyond this value, Reynolds-averaged Navier–Stokes equations with appropriate closure models need to be simulated.

The fluid flow domain of interest is shown in Fig. 11. Theoretically, the far-field boundary condition can be imposed only at infinity. However, in reality, the boundary can be located only at a finite distance. After some numerical experiments, a value of eight times the square prism height was found to be quite satisfactory. The height of the square prism (d) and the velocity at the inflow boundary (V_∞) are used to nondimensionalize length and velocity, respectively. The boundary conditions applied are as follows. The inflow boundary is imposed with a uniform velocity profile ($u = 1.0$, $v = 0.0$). No-slip ($u = v = 0.0$) is enforced on the surface of the prism. A far-field boundary condition ($u = 1.0$, $v = 0.0$) is applied on the lower and upper boundaries of the fluid flow domain to ensure an undisturbed flow. A zero-gradient condition ($\partial u/\partial x = 0$, $\partial v/\partial x = 0$) is applied on the outlet boundary. The flow is started from a quiescent state ($u = v = 0$) and is gradually accelerated to its boundary condition value of $[u(0, y), v(0, y)]^T = [1.0, 0]^T$ in about 1000 iterations.

Grid sensitivity and convergence check. To achieve grid-independent results, computations were performed on two types of fictitious overlapping subdomains, with different grid sizes over two mesh systems. The computational domain is divided into nine subdomains, as shown in Fig. 11 (blocks 1–9). Such a division facilitates a judicious mesh density in zones of special interest, such as the near wake and around the prism walls, where steeper gradients are expected. Only uniform grid spacing can be prescribed within each subdomain. However, this limitation could be easily circumvented by an appropriate subdomain clustering to achieve a nonuniform grid over the whole domain. Thus, division of the downstream region behind the square prism into two subdomains (blocks 8 and 9) has the following advantages: (i) it allows the generation of a finer mesh in the near-wake region (block 8); (ii) a coarse mesh can be used in block 9; and (iii) the outflow boundary can be located in the far downstream. Two finite subdomain mesh systems, FSM V and FSM VI, which are listed in Table VI, were employed with a detailed number of grid points, with uniform grid spacing in each block. The problem of flow past a square prism

TABLE VI
Geometric Parameters and the Mesh Size in Each Block for Flow Past a Square Prism

Block no.	Bottom-left corner location (x_{bl}, y_{bl})	Top-right corner location (x_{tr}, y_{tr})	Number of grid points in	
			FSM V	FSM VI
1	(0.0, 9.5)	(60.0, 16.0)	200 × 70	320 × 120
2	(0.0, 0.0)	(60.0, 6.5)	200 × 70	320 × 120
3	(0.0, 6.5)	(5.0, 9.5)	50 × 40	80 × 50
4	(5.0, 6.5)	(6.0, 9.5)	60 × 80	90 × 120
5	(6.0, 8.5)	(7.0, 9.5)	35 × 60	60 × 90
6	(6.0, 6.5)	(7.0, 7.5)	35 × 60	60 × 90
7	(7.0, 6.5)	(8.0, 9.5)	60 × 80	90 × 120
8	(8.0, 6.5)	(33.0, 9.5)	140 × 60	180 × 70
9	(33.0, 6.5)	(60.0, 9.5)	110 × 40	150 × 50

does not have a steady state solution, as the fluid flow features in the downstream wake region are steady periodic in nature. Hence, it is mandatory to carry out numerical simulations over a long time interval up to $t \geq 40T$. Here, T refers to the period of vortex shedding.

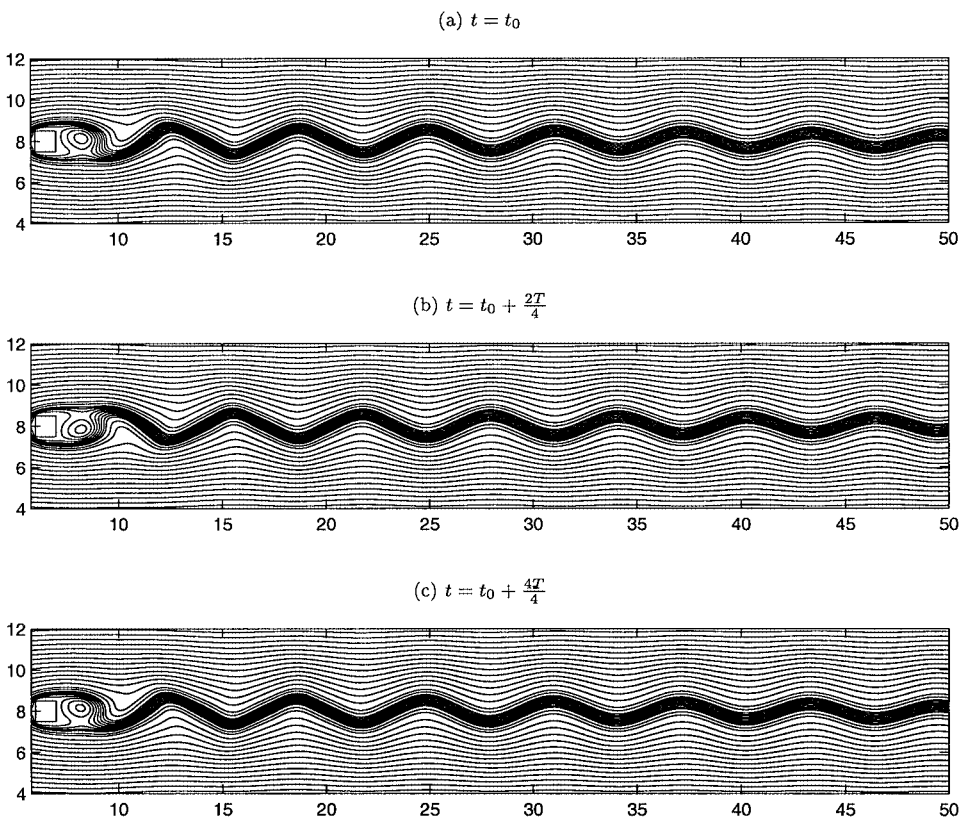

FIG. 12. The streamline contours depicting the wake behind the prism for three successive instants of time over one vortex-sheding period. (a) $t = t_0$; (b) $t = t_0 + \frac{2T}{4}$; (c) $t = t_0 + T$.

Fluid flow features. A Reynolds number value of 100 is chosen to numerically simulate both the quantitative and qualitative fluid flow features. The temporal evolution of the streamline patterns over one complete vortex shedding cycle is depicted in Fig. 12. These streamlines are wavy and sinuous on the leeward side of the square prism. However, the upstream side depicts a potential flowlike pattern. Eddies are formed behind the cylinder and are washed away into the wake region. This phenomenon is popularly known as the Kármán vortex shedding. The visual sequence depicted in Fig. 12 reveals the motion of the eddies. Two eddies are shed within each period from the aft of the square prism. It is noted that Figs. 12a and 12b are half a vortex-shedding cycle apart. The periodic nature of the whole sequence is obvious from Figs. 12a–12c. The corresponding vorticity contours for the above sequence is plotted in Fig. 13. The vorticity contours reveal several additional features which could not be directly perceived from the streamlines. The staggered nature of the Kármán shedding is obvious from these plots. The eddies are alternatively of positive and negative vorticity. This is indeed reflected in the form of crests and troughs in the sinuous wake of the streamlines. Further, to have a better feel for the activity in the near wake, a close-up view is provided in Fig. 14.

The forces acting on the square prism is of design interest, which can be resolved into two components, viz., the drag and the lift. The time histories of drag coefficient (C_d)

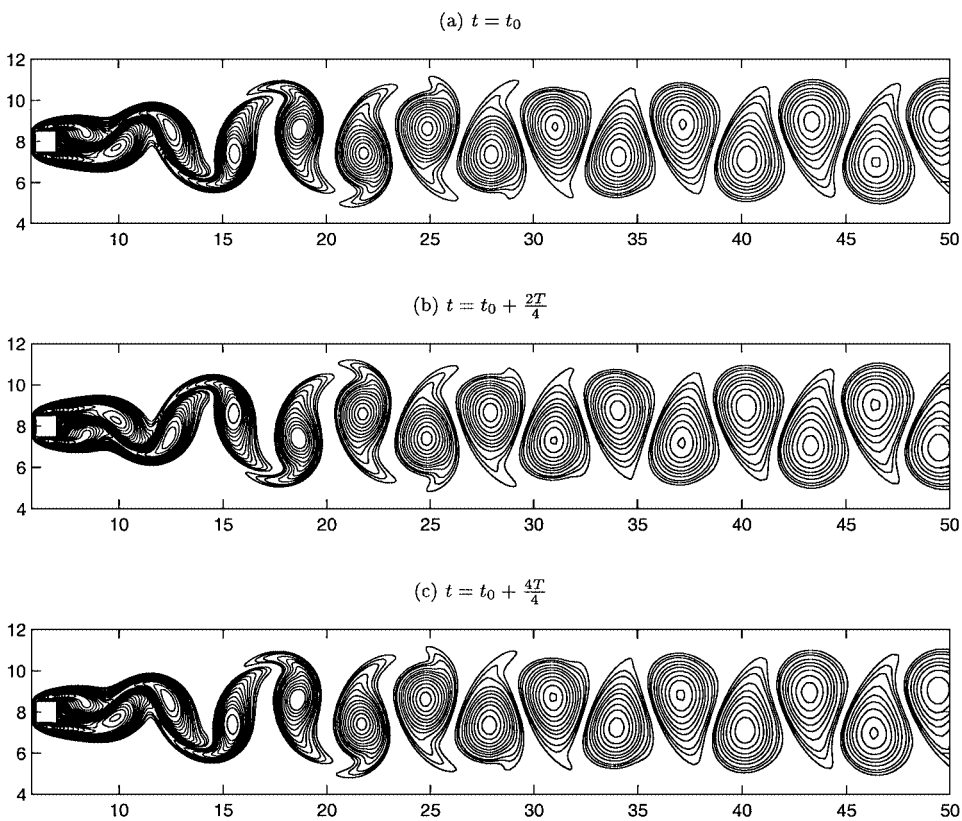

FIG. 13. The vorticity contours depicting the wake behind the prism for three successive instants of time over one vortex-shedding period. (a) $t = t_0$; (b) $t = t_0 + \frac{2T}{4}$; (c) $t = t_0 + T$.

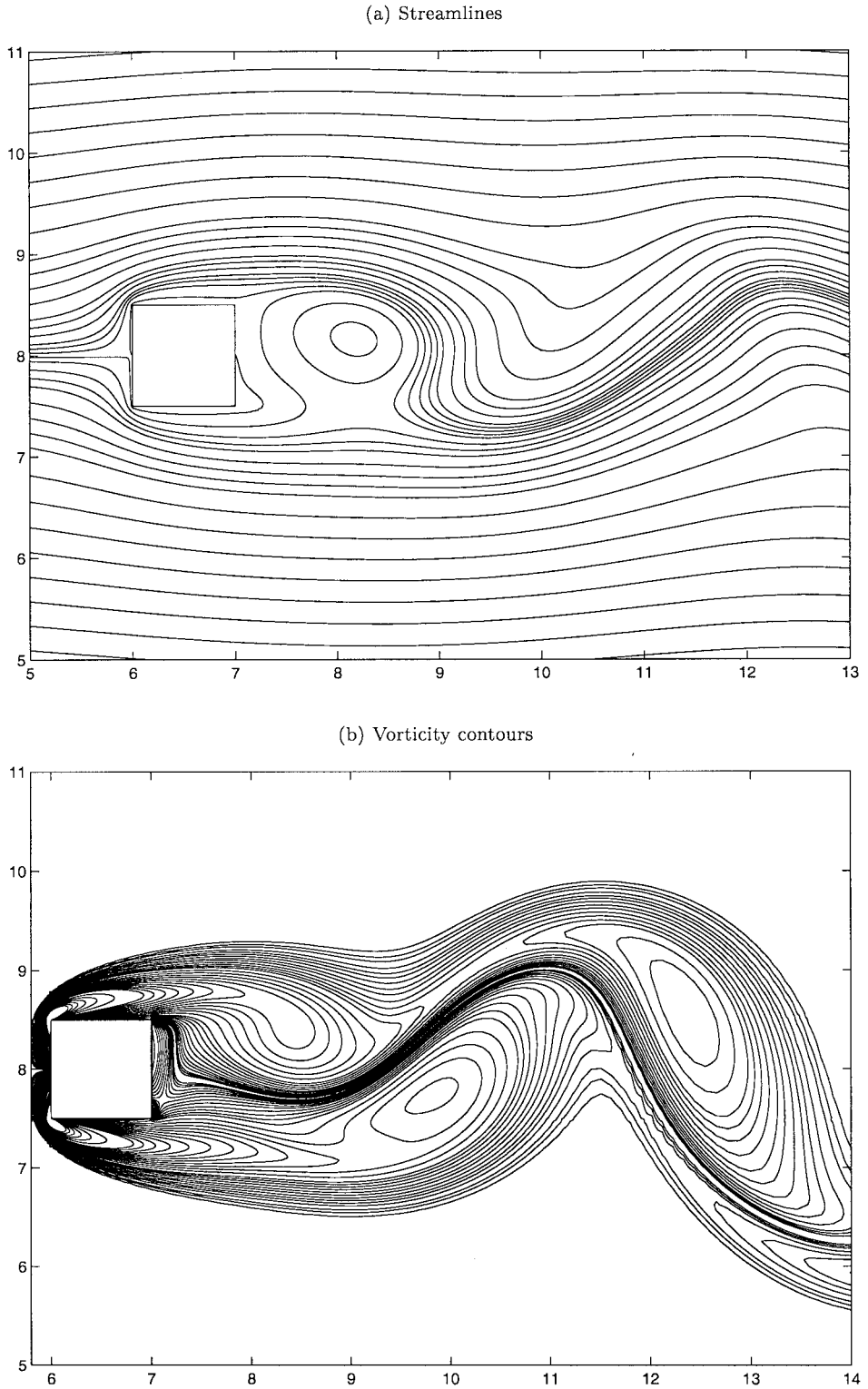

FIG. 14. A close-up view of the fluid flow patterns for flow past a square prism. (a) Streamlines; (b) vorticity contours.

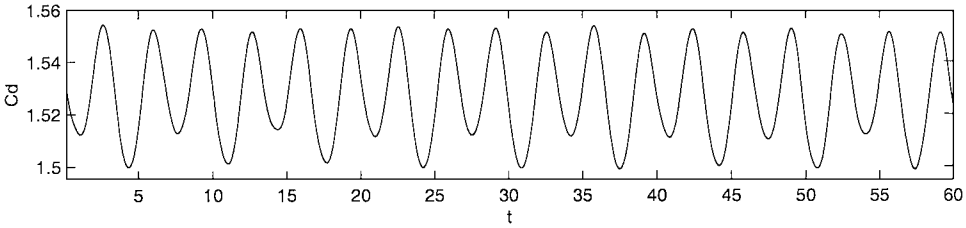

FIG. 15. The time history of the drag coefficient C_d (Re = 100).

and lift coefficient (C_l) are presented in Figs. 15 and 16, respectively. The coefficients C_d and C_l are defined as $F_d/(\frac{1}{2}\rho V_\infty^2 d)$ and $F_l/(\frac{1}{2}\rho V_\infty^2 d)$, respectively, where F_d and F_l refer to the drag and lift forces induced on the square prism. These two forces are in turn obtained by appropriately integrating the contributions of pressure and viscous resistances over the square prism. Here, only a part of the time history spanning close to 10 vortex-shedding cycles is presented. The periodic eddy shedding is reflected in the fluctuating drag coefficient history. From Fig. 15, we can see that there are two local minima (troughs) within each period, which essentially correspond to the two shed eddies. Further, it is observed that the predicted C_d has a higher value than the drag coefficient of a circular cylinder. For the latter case, this value is close to 1.0. The sharp corners of the square prism pose a greater resistance to the flow than could be caused by a circular cylinder. However, in contrast to the drag coefficient, the temporal history of the lift coefficient has only one local minimum. The value of the lift force fluctuation is directly connected to the formation and shedding of the eddy and, therefore, its value varies between a positive maximum and a negative maximum. Table VII summarizes some of the engineering design parameters of special interest, such as the time-averaged drag coefficient ($\bar{C}_d$), the root-mean-square lift coefficient ($C_{l,rms}$), and the Strouhal number (St). Here, $C_{l,rms}$ is defined as $(\overline{C_l^2})^{\frac{1}{2}}$, while the Strouhal number (St) is given by fd/V_∞, where f is the frequency of vortex shedding. As can be observed, the calculated values obtained by DSC–FSM are in good agreement with the earlier investigations. In particular, the calculated St, $C_{l,rms}$, and $\bar{C}_d$ are closer to the recent numerical investigations of Pavlov *et al.* [50]. Nevertheless, it should be mentioned that the predicted value of the Strouhal number is somewhat higher than those obtained in the experiments of Ref. [55]. We surmise that this minor disagreement is mainly due to the local confinement errors in the experiments and the freestream boundary condition of the far field in the computations.

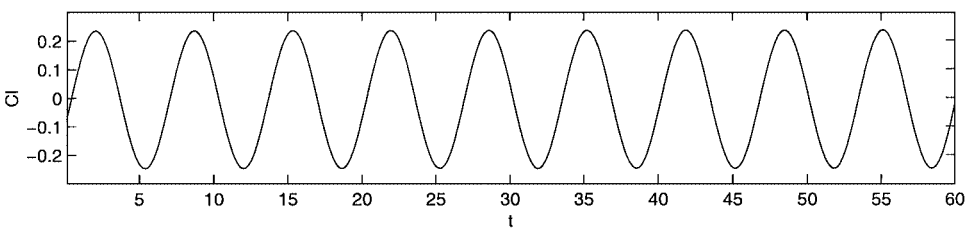

FIG. 16. The time history of the lift coefficient C_l (Re = 100).

TABLE VII
A Comparison of the Engineering Parameters of Interest for Flow Past a Square Prism for Re = 100

	$\bar{C}_d$	$C_{l,rms}$	St
Present study (FSM V)	1.5270	0.1509	0.1532
Present study (FSM VI)	1.5234	0.1483	0.1526
Pavlov *et al.* (Num.) (Ref. [50])	1.51	0.137	0.150
Sohankar *et al.* (Num.) (Ref. [51])	1.46	—	0.149
Arnal *et al.* (Num.) (Ref. [52])	1.42	—	0.153
Li and Humphrey (Num.) (Ref. [53])	1.75	—	0.141
Davis and Moore (Num.) (Ref. [54])	1.63	—	0.151
Okajima (Exp.) (Ref. [55])	—	—	0.135

Note. Exp, experimental; Num, numerical.

IV. CONCLUSIONS

This paper proposes a discrete singular convolution–finite subdomain method (DSC–FSM) for the numerical simulation of viscous incompressible flows. The Navier–Stokes equations are solved over multiply connected complex domains. The DSC–FSM is developed by combining the DSC algorithm [23, 24] with a finite subdomain method (FSM). The DSC kernel performs the dual role of spatial discretization and interpolation (for data transfer) between subdomains. A third-order Runge–Kutta scheme is utilized for the temporal discretization by choosing an optimum time-step size, as dictated by the stability criterion. A fractional-time-step potential-function method (FTS–PEM) [32] is employed for the numerical implementation of Navier–Stokes equations. The successive over relaxation (SOR) scheme is used for solving the Possion equation, which was formulated for the potential function.

Accuracy of the present simulations are validated against the exact solution of the Taylor problem. The robustness of the proposed scheme is verified by simulating the fluid flow features for three standard test problems. The DSC–FSM is tested for both convergence and mesh sensitivity by simulating the flow in a lid-driven cavity even at Re $= 400$. Convergent results were obtained beyond a grid size of 65×65 and for finite subdomain mesh systems FSM I and FSM II. A comprehensive analysis is presented for this problem with extensive validations. Results are also presented at Re $= 5{,}000$ and 10,000. Excellent consistence is obtained with the results available in the literature [44].

The problem of flow over a backward-facing step with two finite subdomain mesh systems in the Reynolds number range of 25–400 is investigated. The evolution of the recirculation region against the Reynolds number is presented in terms of streamlines and vorticity contours. Prediction of reattachment length by DSC–FSM is found to be closer to the experimental results than that obtained by other researchers.

Finally, the laminar flow past a square prism with Re $= 100$ is investigated. The subdomains were judiciously divided to ensure a fine mesh in regions of high velocity gradient, such as the near wake and around the square prism walls. This problem has served as a severe test case to demonstrate the flexibility of the DSC–FSM approach in dealing with complex domains. The von Kármán vortex street, formed behind the square prism, is successfully simulated. A number of parameters of design interest, such as the Strouhal number,

time-averaged drag coefficient, and root-mean-square lift coefficient, are obtained. These values are found to be in good agreement with the earlier investigations.

In summary, the present DSC–FSM method has the following features.

(i) The topological complexity of irregular geometries could be reduced by employing finite subdomains. Thus, computation within each subdomain is relatively independent. This endows the DSC algorithm with greater flexibility in handling truly complex geometries, which is an asset for potential application to complex physical problems, wherein different mathematical models are needed to describe different regions of the computational domain.

(ii) Computational accuracy in each subdomain is controllable. Grid sizes employed in the neighboring subdomains can be independent of each other. This allows arbitrary local grid refinement for handling possible geometric and parametric singularities in the fluid flow system.

(iii) The present DSC–FSM approach can be easily parallelized, which can dramatically enhance the computational efficiency. The present study indicates that the DSC–FSM is an accurate, reliable, and robust approach for dealing with incompressible viscous flows in complex geometries.

ACKNOWLEDGMENTS

This work was supported by the National University of Singapore. The authors thank the anonymous reviewers for their invaluable comments and suggestions.

REFERENCES

1. D. Gottlieb, M. Y. Hussaini, and S. A. Orszag, in *Spectral Methods for Partial Differential Equations*, edited by R. G. Voigt, D. Gottlieb, and M. Y. Hussaini (SIAM, Philadelphia, 1984), p. 0.
2. C. Canuto, M. Y. Hussaini, A. Quarteroni, and T. A. Zang, *Spectral Methods in Fluid Dynamics* (Springer-Verlag, Berlin, 1988).
3. S. A. Orszag, Comparison of pseudospectral and spectral approximations, *Stud. Appl. Math.* **51**, 253 (1972).
4. B. Fornberg, *A Practical Guide to Pseudospectral Methods* (Cambridge Univ. Press, Cambridge, UK, 1996).
5. J. W. Cooley and J. W. Tukey, An algorithm for the machine calculation of complex Fourier series, *Math. Comput.* **19**, 297 (1965).
6. J. S. Walker, *Fast Fourier Transforms* (CRC Press, Boca Raton, FL, 1996).
7. R. Bellman, B. G. Kashef, and J. Casti, A technique for the rapid solution of nonlinear partial differential equations, *J. Comput. Phys.* **10**, 40 (1972).
8. G. E. Forsythe and W. R. Wasow, *Finite-Difference Methods for Partial Differential Equations* (Wiley, New York, 1960).
9. W. T. Tsai and D. K. P. Yue, Computation of nonlinear free-surface flows, *Annu. Rev. Fluid Mech.* **28**, 249 (1996).
10. O. C. Zienkiewicz, *The Finite Element Method in Engineering Science* (McGraw–Hill, London, 1971).
11. J. T. Oden, *Finite Elements of Nonlinear Continua* (McGraw–Hill, New York, 1972).
12. R. T. Fenner, *Finite Element Methods for Engineers* (Imperial College Press, London, 1975).
13. J. N. Reddy, *Energy and Variational Methods in Applied Mechanics* (Wiley, New York, 1984).
14. R. Glowinski and O. Pironneau, Finite element methods for Navier–Stokes equations, *Annu. Rev. Fluid Mech.* **24**, 167 (1992).
15. Y. K. Cheung, *Finite Strip Methods in Structural Analysis* (Pergamon, Oxford, 1976).
16. E. G. Puckett, A. S. Almgren, J. B. Bell, D. L. Marcus, and W. J. Rider, A high-order projection method for tracking fluid interfaces in variable density incompressible flows, *J. Comput. Phys.* **130**, 267 (1997).

17. A. T. Patera, A spectral element methods for fluid dynamics: Laminar flow in a channel expansion, *J. Comput. Phys.* **54**, 468 (1984).
18. H. C. Ku, Solution of flow in complex geometries by the pseudospectral element method, *J. Comput. Phys.* **117**, 215 (1995).
19. A. G. Kravchenko, P. Moin, and K. Shariff, B-spline method and zonal grids for simulations of complex turbulent flows, *J. Comput. Phys.* **151**, 757 (1999).
20. S. A. Orszag, Spectral methods for problems in complex geometries, *J. Comput. Phys.* **37**, 70 (1980).
21. C. D. Dimitropoulos, B. J. Edwards, K. S. Chae, and A. N. Beris, Efficient pseudospectral flow simulations in moderately complex geometries, *J. Comput. Phys.* **144**, 517 (1998).
22. H. H. Yang, B. R. Seymour, and B. D. Shizgal, A Chebyshev pseudospectral multidomain method for steady flow past a cylinder, *Comput. Fluids* **23**, 829 (1994).
23. G. W. Wei, Discrete singular convolution for the solution of the Fokker–Planck equations, *J. Chem. Phys.* **110**, 8930 (1999).
24. G. W. Wei, A unified approach for solving the Fokker–Planck equation, *J. Phys. A* **33**, 343 (2000).
25. G. W. Wei, Solving quantum eigenvalue problems by discrete singular convolution, *J. Phys. B* **33**, 343 (2000).
26. G. W. Wei, A unified method for solving Maxwell's equation, in *Proceedings, Asia-Pacific Microwave Conference*, November 30, 1999, Singapore, p. 562.
27. G. W. Wei, A new algorithm for solving some mechanical problems, *Comput. Methods Appl. Mech. Eng.* **190**, 2017 (2001).
28. G. W. Wei, Vibration analysis by discrete singular convolution, *J. Sound Vib.* **244**, 535 (2001).
29. G. W. Wei, Discrete singular convolution method for the sine–Gordon equation, *Physica D* **137**, 247 (2000).
30. M. J. Ablowitz, B. M. Herbst, and C. Schober, On numerical solution of the sine–Gordon equation, *J. Comput. Phys.* **126** (1996).
31. S. Guan, C.-H. Lai, and G. W. Wei, Fourier–Bessel analysis of patterns in a circular domain, *Physica D* **151**, 83 (2001).
32. D. C. Wan, Y. C. Zhou, and G. W. Wei, Numerical solutions for unsteady incompressible flow using discrete singular convolution method, *Int. J. Numer. Methods Fluids* **38**, 789 (2002).
33. D. C. Wan and G. W. Wei, Numerical study of Euler and Navier–Stokes equations by efficient discrete singular convolution method, *ACTA Mech. Sin.* **16**, 223 (2000).
34. G. W. Wei, Quasi wavelets and quasi interpolating wavelets, *Chem. Phys. Lett.* **296**, 215 (1998).
35. L. S. Caretto, A. D. Gosman, S. V. Patankar, and D. B. Spalding, Two calculation procedures for steady, three-dimensional flows with recirculation, in *Proc. Third Int. Conf. Numer. Methods Fluid Dyn., Paris, 1972*.
36. P. J. Zwart, G. D. Raithby, and M. J. Raw, The integrated space–time finite volume method and its application to moving boundary problems, *J. Comput. Phys.* **154**, 497 (1999).
37. S. V. Patankar, *Numerical Heat Transfer and Fluid Flow* (McGraw–Hill, New York, 1980).
38. C. A. J. Fletcher, *Computational Techniques for Fluid Dynamics—Fundamental and General Techniques* (Springer-Verlag, Berlin/New York, 1988).
39. F. H. Harlow and J. E. Welcch, Numerical study of large amplitude free surface motion, *Phys. Fluids* **9**, 842 (1966).
40. A. J. Chorin, A numerical method for solving incompressible viscous flow problems, *J. Comput. Phys.* **135**, 118 (1997).
41. R. Peyret and T. D. Taylor, *Computational Methods for Fluid Flow*, Springer Series in Computer Physics (Springer-Verlag, Berlin/Heidelberg, 1980).
42. P. N. Shankar and M. D. Deshpande, Fluid mechanics of the driven cavity, *Annu. Rev. Fluid Mech.* **32**, 93 (2000).
43. T. E. Tezduyar, J. Liou, D. K. Ganjoo, and M. Behr, Solution techniques for the vorticity-streamfunction formulation of 2-dimensional unsteady incompressible flows, *Int. J. Numer. Methods Fluids* **11**, 515 (1990).
44. U. Ghia, K. N. Ghia, and C. T. Shin, High-Resolutions for incompressible flow using the Navier–Stokes equations and a multigrid method, *J. Comput. Phys.* **48**, 387 (1982).

45. A. Campion-Rrenson and M. J. Crochet, On the streamfunction-vorticity finite element solutions of Navier–Stokes equations, *Int. J. Numer. Methods Eng.* **12**, 1809 (1978).
46. S. Ozawa, Numerical studies of steady flow in a two-dimensional square cavity at high Reynolds numbers, *J. Phys. Soc. Jpn.* **38**, 889 (1975).
47. B. F. Armaly, F. Durst, J. C. F. Pereira, and B. Schoung, Experimental and theoretical investigation of backward-facing step flow, *J. Fluid Mech.* **127**, 473 (1983).
48. J. A. Sethian and A. F. Ghoniem, Validation-study of vortex methods, *J. Comput. Phys.* **74**, 283 (1988).
49. J. Y. Zhu, The 2nd-order projection method for the backward-facing step flow, *J. Comput. Phys.* **117**, 318 (1995).
50. A. N. Pavlov, S. S. Sazhin, R. P. Fedorenko, and M. R. Heikal, A conservative finite difference method and its application for the analysis of a transient flow around a square prism, *Int. J. Numer. Methods Heat Fluid Flow* **10**, 6 (2000).
51. A. Sohankar, C. Norberg, and L. Davidson, Low-Reynolds-number flow around a square cylinder at incidence: Study of blockage, onset of vortex shedding and outlet boundary condition, *Int. J. Numer. Methods Fluids* **26**, 39 (1998).
52. M. P. Arnal, D. J. Goering, and J. A. C. Humphrey, Vortex shedding from a bluff body adjacent to a plane sliding wall, *J. Fluids Eng.* **113**, 384 (1991).
53. G. Li and J. A. C. Humphrey, Numerical modeling of confined flow past a cylinder of square cross-section at various orientations, *Int. J. Numer. Methods Fluids* **20**, 1215 (1995).
54. R. W. Davis and E. F. Moore, A numerical study of vortex shedding from rectangles, *J. Fluid Mech.* **116**, 474 (1982).
55. A. Okajima, Strouhal numbers of rectangular cylinders, *J. Fluid Mech.* **123**, 379 (1982).
56. C. H. K. Williamson, Vortex dynamics in the cylinder wake, *Annu. Rev. Fluid Mech.* **28**, 477 (1996).
57. M. Breuer, J. Bernsdorf, T. Zeiser, and F. Durst, Accurate computations of the laminar flow past a square cylinder based on two different methods: Lattice-Boltzmann and finite volume, *Int. J. Heat Fluid Flow* **21**, 186 (2000).